

Impact of superlinear defect-related recombination on LED performance at low injection

Cite as: J. Appl. Phys. **125**, 204502 (2019); <https://doi.org/10.1063/1.5089125>

Submitted: 16 January 2019 . Accepted: 02 May 2019 . Published Online: 29 May 2019

T. H. Gfroerer, Ruiming Chen, Grace Watt , Zhiqiang Liu , and Yong Zhang 



View Online



Export Citation



CrossMark



Alluxa YOUR OPTICAL COATING PARTNER  **DOWNLOAD THE LIDAR WHITEPAPER**

Impact of superlinear defect-related recombination on LED performance at low injection

Cite as: J. Appl. Phys. **125**, 204502 (2019); doi: [10.1063/1.5089125](https://doi.org/10.1063/1.5089125)

Submitted: 16 January 2019 · Accepted: 2 May 2019 ·

Published Online: 29 May 2019



View Online



Export Citation



CrossMark

T. H. Cfroerer,^{1,a)} Ruiming Chen,¹ Grace Watt,^{1,b)}  Zhiqiang Liu,²  and Yong Zhang³ 

AFFILIATIONS

¹Davidson College, Davidson, North Carolina 28035, USA

²Institute of Semiconductors, Chinese Academy of Science, Beijing 100086, China

³University of North Carolina at Charlotte, Charlotte, North Carolina 28223, USA

^{a)}Email: tigfroerer@davidson.edu

^{b)}Present address: Center for Power Electronics at Virginia Tech, Blacksburg, Virginia 24061, USA.

ABSTRACT

We investigate the temperature and injection dependence of the electroluminescence from an InGaN/GaN LED to characterize the defect-related recombination mechanism in this system. In contrast to the standard ABC recombination model, we show that the defect-related recombination rate varies superlinearly with carrier density. The elevated loss rate with injection indicates that defect states are less detrimental at low injection, only becoming available for occupation via carrier delocalization or more dynamic Shockley–Read–Hall statistics. This characteristic alleviates defect-related losses by making the radiative mechanism more competitive such that high dislocation density devices can perform better at low injection.

Published under license by AIP Publishing. <https://doi.org/10.1063/1.5089125>

I. INTRODUCTION

Light emitting diodes (LEDs) are quickly superseding other forms of lighting because they are more efficient and more reliable than other technologies. However, InGaN/GaN-based blue LEDs, which are typically required for general purpose white lighting applications, suffer from a phenomenon commonly known as quantum efficiency droop. When the LED is driven by a current exceeding a specific threshold, the efficiency of conversion from electrical to optical power decreases. Since this shortcoming limits the ultimate performance of high brightness LEDs, the efficiency droop in blue LEDs has been the subject of vigorous research. Over time, a wide variety of physical mechanisms and potential remedies have been proposed.^{1,2} While some groups have asserted that they have identified the dominant droop mechanism,³ others have disputed these claims.⁴ Hence, the topic remains more or less unresolved.

Meanwhile, the efficiency of these devices in the intermediate injection regime often exceeds expectations.⁵ Despite the presence of threading dislocation densities on the order of 10^9 cm^{-2} and corresponding Shockley–Read–Hall (SRH) nonradiative recombination

coefficients A on the order of 10^8 s^{-1} , highly efficient radiative emission is observed.⁶ While A increases with dislocation density, confirming that dislocations act as nonradiative recombination centers, photoluminescence lifetimes independent of threading dislocation density have also been reported.⁷ These results have generally been explained by localization effects in the InGaN quantum wells (QWs),⁸ which limit access to both point and extended defects.⁹ Similar behavior is observed in other systems,¹⁰ where reduced carrier mobility leads to improved radiative recombination efficiency.

In this contribution, we report temperature- and injection-dependent measurements of the integrated electroluminescence (EL) from an InGaN/GaN quantum well-based high brightness blue LED. We observe a sharp increase in the nonradiative recombination rate R_{nr} when the injection exceeds a temperature-dependent threshold, signaling the onset of droop. Below this threshold, we obtain nonradiative recombination rates that increase superlinearly with electron–hole pair density. In particular, in the 150–300 K temperature regime, the nonradiative recombination results are surprisingly consistent,

following an extremely simple power law relationship with carrier density.

Under very special circumstances, Shockley–Read–Hall statistics¹¹ yield a defect-related recombination rate that scales linearly with carrier density such that the rate can be adequately described by a proportionality coefficient A . More specifically, if the participating defect levels are deep enough, then thermal excitation of electrons and holes out of these levels can be neglected. Furthermore, if the injected density of electrons equals the density of holes, both exceeding background concentrations, and trap capture times do not vary with trap energy, the SRH integral across the defect level distribution can be evaluated analytically. This calculation results in a recombination rate R_{SRH} that is proportional to the product of the defect density N and free carrier density n and inversely proportional to the effective capture time τ , which is the sum of the electron and hole capture times: $R_{\text{SRH}} = An$ with $A = \frac{N}{\tau}$.

This SRH simplification, which relies on a host of unverified assumptions, facilitates the standard ABC recombination model,^{12–14} $R_{\text{net}} = An + Bn^2 + Cn^3$, where R_{net} is the net recombination rate, B is the bimolecular radiative recombination coefficient, and C is the Auger recombination coefficient. While Auger mechanisms may contribute to the nonradiative loss in the high-density regime, we are primarily interested in the low to intermediate carrier density ($n \leq 10^{17} \text{ cm}^{-3}$) behavior where 3-particle Auger contributions can be safely neglected. Here, we are left with two competing recombination mechanisms: nonradiative SRH and radiative recombination. Assuming bimolecular (i.e., 2-particle, electron and hole) band-to-band radiative recombination, our analysis identifies a significant deficiency in the ABC recombination model. Namely, as noted above, the nonradiative recombination rate increases superlinearly with carrier density. This result indicates that the SRH recombination lifetime and coefficient A are not independent of carrier injection, as is typically assumed. Rather, the SRH lifetime decreases systematically with increasing carrier concentration. In other material systems, this phenomenon has been explained by a specific characteristic of the defect level distribution: the defect-related density of states increases with proximity to the band edges.^{15,16} However, since the SRH model only describes bulk materials with unrestricted mobility, which is an invalid description of our system, carrier delocalization,⁹ leakage,¹² or tunneling¹⁴ with increasing carrier density may also contribute to the superlinear (SL) relationship in our QW device.

II. EXPERIMENT

The InGaN/GaN multiple QW (MQW) blue LED under investigation here was grown on a c -plane sapphire substrate and has a room temperature peak emission wavelength near 450 nm. Representative details of the specific device structure and fabrication procedure can be found elsewhere.^{9,17} The EL spectrum, measured with an Ocean Optics USB2000 UV-VIS spectrometer, changes very little with temperature between 100 K and 300 K as shown in Fig. 1. Low-temperature ($T < 77$ K) measurements for calibrating the quantum efficiency are conducted in a Janis CCS-400H/204N closed-cycle refrigerator system. For higher accuracy measurements at temperatures $T \geq 77$ K, the 1 mm^2 device is mounted in an Oxford Instruments Optistat DN static exchange gas cryostat. Since the Janis system employs a cold finger in

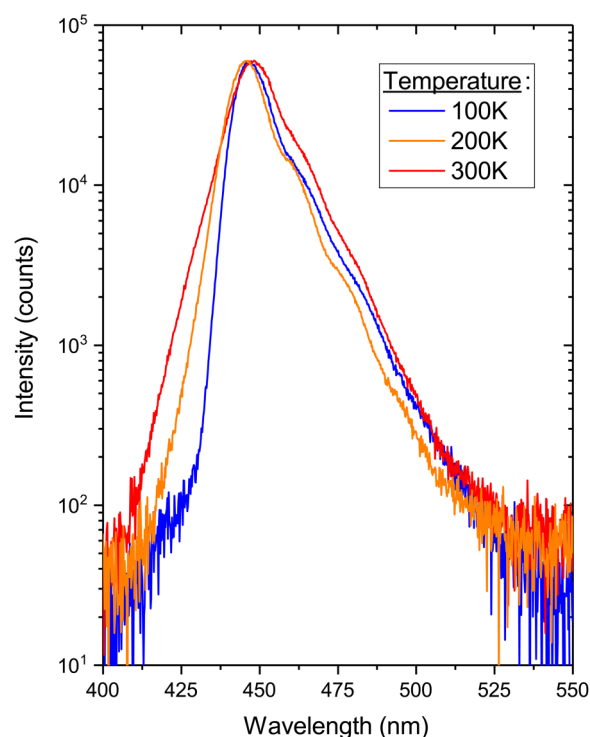


FIG. 1. EL spectra at an injection current density of 1 mA/cm^2 . Spectral acquisition times were 400 ms at 100 K, 800 ms at 200 K, and 1800 ms at 300 K.

vacuum configuration, the exchange gas in the Oxford cryostat provides better thermal stability. A Keithley 2400 SourceMeter is used to set the drive current, and the spectrally-integrated electroluminescence is directed onto a New Focus 2031 Large-Area Photoreceiver. No optical filters are employed, so the photoreceiver signal includes all EL emission within the 400–1070 nm response curve of the Silicon detector.

For this type of experiment, low duty cycle pulsed-current operation is generally preferred to minimize self-heating in the device.¹⁸ Nevertheless, our EL signal is obtained in a quasi-steady-state condition to better approximate normal operation and to maintain compatibility with complementary imaging measurements, which have been reported separately.¹⁹ We activate the current output on the SourceMeter, record the photoreceiver voltage, and then deactivate the current output. In most of the experimental conditions under investigation here, the photoreceiver voltage is stable and heating effects can be safely neglected. However, we do observe voltage drift when higher currents are applied at low temperature. Since we need to omit these measurements from our analysis, this mode of data acquisition limits our operational parameter space.

III. RESULTS

We compute the relative internal quantum efficiency (IQE) by taking the ratio of the photoreceiver output voltage and the LED

source current. Since the EL emission is not directional and not all emitted light is captured by the photoreceiver, we calibrate the relative IQE by assuming that the maximum response (obtained at the lowest injection point $J = 0.02 \text{ mA/cm}^2$ and lowest temperature $T = 10 \text{ K}$) corresponds to unity IQE and all measurements are normalized to this limiting response. Representative results of this commonly accepted normalization procedure²⁰ are shown in Fig. 2 (for $T = 10\text{--}150 \text{ K}$) and Fig. 3 (for $T = 100\text{--}300 \text{ K}$). The closed symbols in Fig. 2 show the results for measurements in the closed-cycle refrigerator. Phenomenologically, the low-temperature asymptotic behavior follows the relationship $\text{IQE} = 1 - 0.043 \times J^{0.39}$, which is represented by the dashed line in Fig. 2. The open symbols in Figs. 2 and 3 denote measurements made in the static exchange gas cryostat, which are scaled to match the refrigerator measurements at 150 K. We find that small corrections (on the order of 10%) to this normalization method have little impact on the principal outcomes of this study.

The room temperature external quantum efficiency of this device is 37.6% at $3.5 \times 10^4 \text{ mA/cm}^2$ without encapsulation. Meanwhile, our calibration procedure indicates an IQE of approximately 70% at this temperature and current density. These results point to a light extraction efficiency exceeding 50%, which is

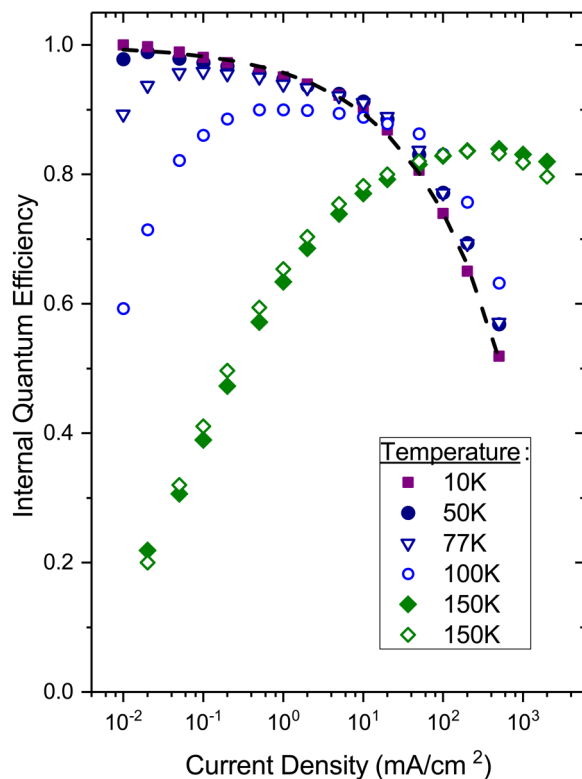


FIG. 2. IQE vs current density in the test device. The closed symbols are measurements in the Janis refrigerator, the open symbols are measurements in the Oxford cryostat, and the dashed line is a phenomenological fit to the low-temperature results.

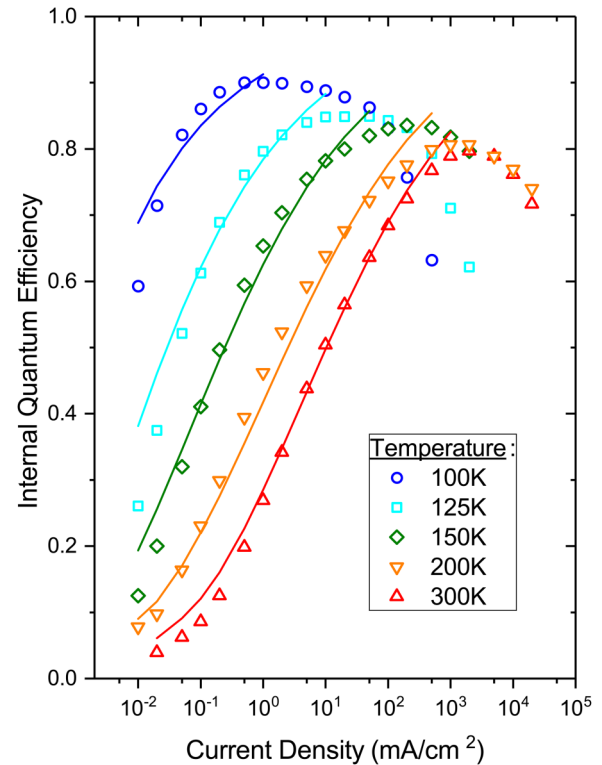


FIG. 3. IQE vs current density in the test device. The open symbols are Oxford cryostat measurements and the lines represent modeling results.

generally consistent with other estimates for similar unencapsulated planar devices that contain a photonic scattering structure.²¹

When nonradiative mechanisms are significant, density-dependent changes in the underlying recombination rates produce IQE curves that increase, decrease, or sometimes change nonmonotonically between the two with increased injection, which we observe at temperatures $T \geq 50 \text{ K}$. For SRH recombination, these trends are generally driven by occupation-related saturation effects, where the behavior may differ for point and extended defects.²² SRH recombination can also be thermally activated, such that the SRH mechanism is frozen out at low temperature.¹⁸ Indeed, for $T < 50 \text{ K}$, we observe a temperature-independent IQE response curve that asymptotically approaches a consistent maximum level with decreasing current density J . Asymptotic IQE response indicates that nonradiative mechanisms are becoming less and less competitive with the radiative process at low injection. These observations, which are generally consistent with other studies,²⁰ further justify our normalization procedure.

For $T < 50 \text{ K}$, the IQE is highest at the minimum injection level (10^{-2} mA/cm^2) and decreases steadily with increasing injection, indicating that SRH-type nonradiative recombination is very weak at low temperature in this device. The observed behavior differs substantially from a comparable study,²⁰ where the device required injection on the order of 100 mA/cm^2 to saturate the SRH

mechanism and reach peak efficiency at 25 K. IQE vs J curves above 50 K reflect the interplay of thermally activated defect-related recombination, radiative recombination, and the droop mechanism. In the intermediate temperature range $77\text{ K} < T < 100\text{ K}$ where non-radiative recombination begins to appear at low injection, the droop mechanism continues to follow the low-temperature trend, but the droop onset begins to shift to higher-injection thresholds. With further increase in temperature, higher currents are tolerated in the device before droop becomes apparent, but defect-related recombination continues to pull the low-injection efficiency down, so the peak IQE drops systematically.

Both phenomena can be attributed to thermally-activated carrier delocalization, which has recently been demonstrated via inhomogeneous EL imaging in this temperature regime.¹⁹ If we assume that the droop mechanism is primarily a function of the local carrier density, delocalization reduces the droop injection threshold by spreading the carriers more uniformly across the device. Meanwhile, thermally activated delocalization can augment defect-related recombination by giving the released carriers access to more nonradiative centers.⁹ Competition with thermally activated SRH recombination also pushes the apparent droop threshold to higher current with increasing temperature.

It has been shown that radiative recombination in polar InGaN/GaN QWs grown on c -plane sapphire substrates is bimolecular, meaning that excitonic effects can be neglected.²³ Since our LEDs are grown this way, we assume that the radiative recombination rate in the active QWs is equal to Bn^2 , where $B_{300} = 1 \times 10^{-10}\text{ cm}^3\text{ s}^{-1}$ is the radiative recombination coefficient at room temperature (300 K) and n is the photoexcited carrier density.^{5,6,12} We note that this estimate for B includes corrections that are required to accommodate photon recycling,²⁴ which will vary with device structure and optical design. This expression for the radiative rate assumes that the generated electron-hole density exceeds the background density of free carriers in the active region of the device, a condition that may be suspect for our lowest generation rates. The relatively small bandgap dependence of B is neglected in this study.

The temperature dependence of the radiative recombination coefficient B in InGaN/GaN QWs has not been definitely established. In III-V semiconductors, it has generally been assumed that $B(T) \propto T^{-3/2}$ in the bulk^{25,26} and $B(T) \propto T^{-1}$ in 2-dimensional QWs.²⁷ However, Gerber and Kleinman have recently argued that $B(T) \propto T^{-2}$ in bulk GaAs.²⁸ Moreover, recent studies of InGaN-based QWs have reached widely divergent conclusions, with one study²⁹ reporting $B(T) \propto T^{-7/4}$ and another¹³ suggesting that B actually increases with T . The discrepancies can probably be attributed to the ambiguity between thermally activated SRH recombination and the temperature dependence of B . Assuming that B is inversely related to T , both phenomena yield qualitatively similar behavior: SRH recombination gains strength relative to radiative recombination as the temperature is increased, shifting the rising edge of the IQE curve to higher current density.

Quantitatively, we should be able to distinguish the 2 mechanisms because thermal activation is exponential while $B(T)$ follows a power law relationship. For example, our experimental results cannot be reconciled with pure thermal activation of SRH recombination and a radiative coefficient that is independent of B .

Supplementary information from other measurements, like the delocalization activation energy obtained via EL imaging, can also guide our analysis. With these constraints, we find that $B(T) \propto T^{-3/2}$ provides the best match with experimental observations. We cannot rule out similar possibilities like $B(T) \propto T^{-1}$ or $B(T) \propto T^{-2}$, but these relations produce inferior agreement with our temperature-dependent IQE curves and our prior measurement¹⁹ of the delocalization activation energy: 37 meV.

The internal quantum efficiency is the ratio of the radiative and net recombination rates,

$$\text{IQE} = \frac{B(T)n^2}{R_{\text{net}}}, \quad (1)$$

where the total recombination rate is the sum of the radiative and nonradiative contributions: $R_{\text{net}} = Bn^2 + R_{nr}$, with R_{nr} being the nonradiative recombination rate. If we assume that $B(T) \propto T^{-3/2}$ and R_{nr} is thermally activated SRH recombination, we get

$$\text{IQE}(T) = \frac{B_{300} \left(\frac{300}{T}\right)^{3/2} n^2}{B_{300} \left(\frac{300}{T}\right)^{3/2} n^2 + R_{\infty} e^{-E_a/k_B T}}, \quad (2)$$

where R_{∞} is the SRH recombination rate at infinite temperature and k_B is Boltzmann's constant. If we further neglect the temperature dependence of the injected carrier density n at fixed J , Eq. (2) simplifies to

$$\text{IQE}(T) = \frac{1}{1 + C_a T^{3/2} e^{-E_a/k_B T}}, \quad (3)$$

where C_a is a constant fitting parameter. Rearranging Eq. (3) yields

$$\left(\frac{1}{\text{IQE}} - 1\right) T^{-3/2} = C_a e^{-E_a/k_B T}. \quad (4)$$

Figure 4 is an Arrhenius plot of the left-hand side (LHS) of Eq. (4) for $77\text{ K} \leq T \leq 200\text{ K}$ at $J = 10^{-2}\text{ mA/cm}^2$. The analysis yields an SRH activation energy of 34 meV, which closely matches our independent estimate of the delocalization activation energy in this device. Alternative forms of $B(T)$, like $B(T) \propto T^{-1}$ or $B(T) \propto T^{-2}$, produce SRH activation energies that are too large or too small relative to the delocalization energy, respectively.

In steady state, the generation rate G equals the net recombination rate R_{net} , so we can write the internal quantum efficiency as follows: $\text{IQE} = Bn^2/R_{\text{net}} = Bn^2/G$. We use the forward current to compute the electrical generation rate: $G_{\text{elec}} = I/(e a d)$, where I is the measured current, e is the electron charge, $a = 1\text{ mm}^2$ is the device area, and $d = 6\text{ QWs} \times 3\text{ nm/QW} = 18\text{ nm}$ is the active device thickness. Including all 6 QWs in the active volume deviates from prior analysis,¹² where recombination was assumed to occur in a single well, and relies on a more recent report,¹⁴ which indicates that injected electrons and holes are uniformly distributed throughout the MQW region.

Combining experimental estimates of G and IQE with $B(T) \propto T^{-3/2}$, we can calculate the carrier density $n = \sqrt{G \cdot \text{IQE}/B(T)}$ and the nonradiative recombination rate $R_{nr} = G - Bn^2$. The results of this analysis are represented by open

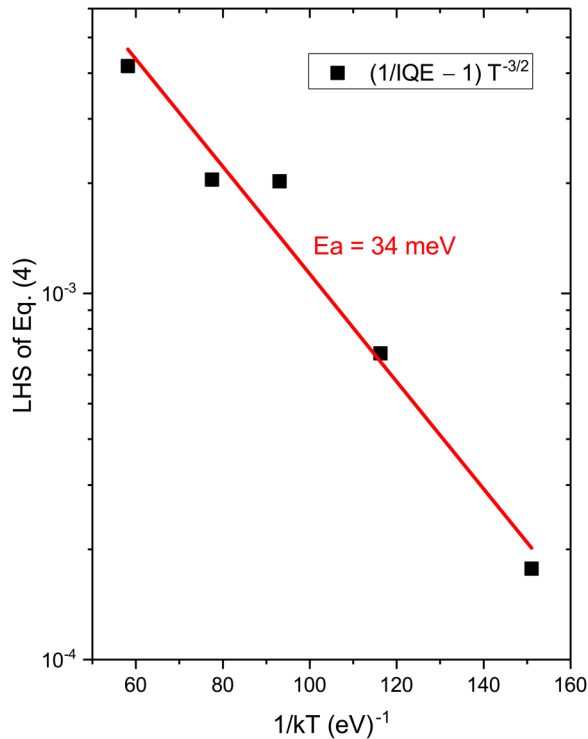


FIG. 4. Arrhenius plot of the left-hand side of Eq. (4) at our minimum injection current of 10^{-2} mA/cm². The slope yields an SRH recombination thermal activation energy of 34 meV.

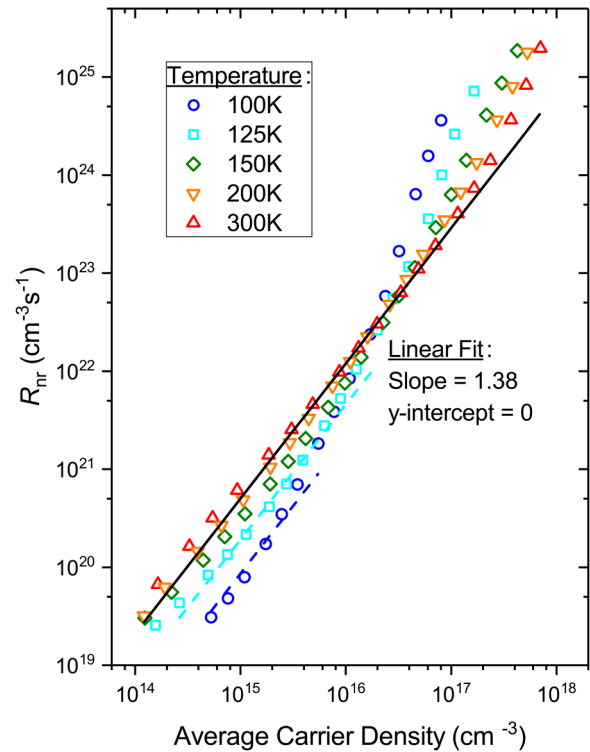


FIG. 5. Nonradiative recombination rate vs carrier density. The open symbols are experimental results, the solid black line is the average linear fit for $n < 10^{17}$ cm⁻³ and $T \geq 150$ K, and the dashed lines represent thermal corrections to the average linear fit at 100 K and 125 K.

symbols in the log–log plot of Fig. 5. Anomalous behavior is observed below 150 K where the SRH mechanism is frozen out.¹⁸ For $150\text{ K} < T < 300\text{ K}$, where SRH recombination is thermally activated, we observe a steady slope equal to 1.38 for $n < 10^{17}$ cm⁻³, independent of temperature. We find it particularly surprising that the y-intercept of this linear fit is exactly zero, so the superlinear (SL) coefficient $A_{SL} = 1\text{ s}^{-1}$: $R_{nr} = A_{SL} n^{1.38} = n^{1.38}\text{ s}^{-1}$. The linearity of the log–log plot demonstrates a remarkably uniform exponential relationship between the nonradiative rate and carrier density in this regime. Above $n = 10^{17}$ cm⁻³, we observe the onset of droop where the nonradiative recombination rate increases much more rapidly with carrier density.

The superlinearity of the SRH rate can be explained by a deficit of defect states when carriers are localized and an increasing density of accessible defect sites when localized levels are filled and carriers have energies approaching the conduction and valence band edges. A defect level distribution with increasing abundance near the band edges means that more defect states are available for occupation as the quasi-Fermi levels move through these energies. The behavior can be represented phenomenologically by a nonradiative recombination rate with a superlinear density dependence. Since the exponent 1.38 remains smaller than the radiative recombination exponent, which equals 2, radiative recombination is still faster at high carrier density. However, the augmented SRH exponent produces a slower transition between the low-injection,

defect-dominated and higher-injection, radiation-dominated recombination regimes.¹⁵

Using the experimentally deduced nonradiative rates, we can determine IQE vs G prior to the onset of droop. A representative example of this calculation is shown in Fig. 6 for $T = 200$ K. The solid line uses the exponential density dependence of R_{nr} obtained from Fig. 5, while the dashed line assumes a defect-related recombination rate that varies linearly with carrier density (with $A = 9 \times 10^5\text{ s}^{-1}$). This value of A produces a theoretical curve that passes through the central portion of the data, while smaller or larger values yield similar curves shifted to the right or left of the experimental results, respectively. The superior fit of the model with the increased exponent indicates that higher carrier densities amplify SRH recombination in this regime. This conclusion is qualitatively consistent with the density-activated defect recombination model, which postulates the onset of a quadratically increasing loss rate when the carrier density saturates low-lying states.²⁹

IV. DISCUSSION

The temperature dependence of the onset of IQE droop at high excitation is consistent with previously reported behavior.^{20,29} The

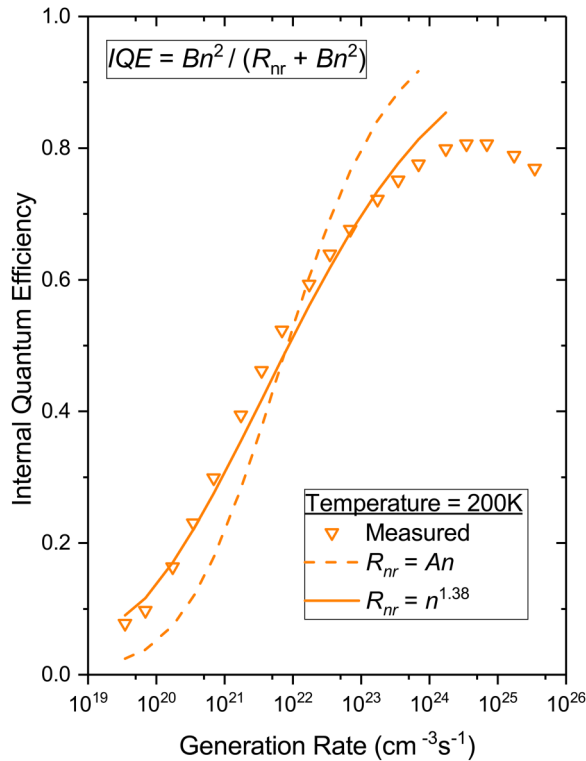


FIG. 6. IQE vs G at 200 K. The dashed and solid lines represent theoretical predictions for SRH recombination that vary linearly and superlinearly with carrier density, respectively.

reduced injection threshold for IQE droop with decreasing temperature reflects the combined effects of SRH recombination and unidentified droop mechanisms with low-temperature localization. At 100 K, localization strongly inhibits SRH recombination by limiting access to nonradiative centers. Meanwhile, carriers are restricted to low energy channels where the effective local carrier density is much higher. Hence, droop is the primary loss mechanism, with an early onset of approximately 1 mA/cm². Delocalization with increasing temperature activates the superlinear SRH recombination mechanism and spreads the carriers more uniformly throughout the active region. These effects increase nonradiative loss at low injection levels and push the IQE maximum to higher measured densities, resulting in higher droop thresholds with increasing temperature.

For $T < 200$ K, Fig. 4 shows that SRH recombination is thermally activated with an activation energy $E_a = 34$ meV. Assuming that SRH recombination is fully activated at approximately 180 K, we can use this activation energy estimate to compute the reduced rates at lower temperatures,

$$R_{SRH} = \frac{e^{-E_a/k_B T}}{e^{-E_a/(k_B \cdot 180 \text{ K})}} \times n^{1.38}. \quad (5)$$

Applying this correction to the 100–125 K measurements, we obtain the dashed lines in Fig. 5. Agreement at moderately low

current density is improved, but early onset droop produces a much steeper carrier density dependence with increasing injection.

Now, using $R_{SRH} = n^{1.38} \text{ s}^{-1}$ for $T \geq 150$ K and applying the thermally corrected superlinear estimates for lower temperatures, we can predict the IQE curves at all temperatures. The results of this analysis yield the solid line efficiency curves in Fig. 3. For such a simple model, the agreement with measured values across such a broad range of temperatures and injection levels is remarkably good. Our approach is further confirmed by considering the remainder of the nonradiative recombination in the high injection regime. In Fig. 7, we plot the difference between the measured nonradiative recombination and the superlinear SRH approximation: $R_D = R_{nr} - R_{SRH}$. We find that R_D adheres closely to a power law relationship: $R_D \propto n^\beta$, with exponent β increasing systematically with temperature. Since an erroneous treatment of SRH would produce artifacts in the nonradiative recombination that is attributed to droop, the systematic exponential increase in the droop-related recombination rate R_D provides additional evidence that the SRH rate is handled correctly. While the subcubic density dependence is technically inconsistent with 3-particle Auger recombination as the dominant droop mechanism, droop mechanisms with supercubic density dependence have been widely reported.^{12,14} We hesitate to speculate further on the physical meaning of these slopes, given our mode of data acquisition and the associated potential for local heating in the high injection regime.

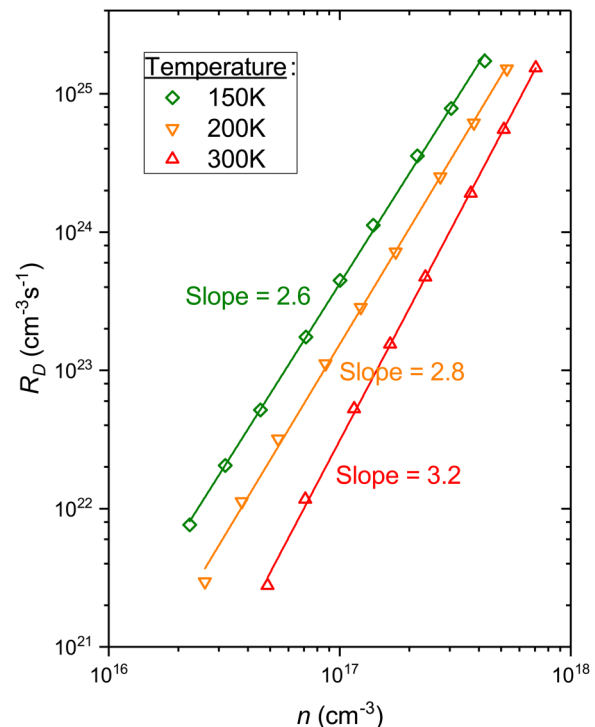


FIG. 7. Droop recombination rate vs carrier density in the high injection regime. The solid lines are linear fits with slopes as shown.

V. CONCLUSION

Defect-related nonradiative recombination in semiconductors is usually assumed to be linear with carrier density (i.e., $R_{\text{SRH}} = An$). In contrast, we find defect rates that increase superlinearly with density in InGaN/GaN QWs. The superlinear behavior may be due to the presence of Urbach-like tails³⁰ on the conduction and valence bands, where the density of defect levels increases as the trap energy approaches the mobile band edge states. In this scenario, the SRH mechanism gains strength with injection because more defect levels become available as the quasi-Fermi energies move toward the band edges. Alternatively, the superlinearity may arise from density-driven delocalization, which permits carriers to be captured by nonradiative centers further from localization sites. Here, the increasing carrier density saturates localized low-lying states so that carriers spill over into less favorable regions of the device.

Either way, the IQE in the low-injection regime is enhanced. This conclusion is counter-intuitive, because a superlinear nonradiative recombination mechanism increases more quickly with injection. However, the underlying physical behavior actually involves a delay in the onset of SRH recombination with increasing carrier density. This change in the carrier dynamics allows the radiative mechanism to compete more successfully with SRH, because SRH is weaker at a low carrier density where the radiative rate is slower and more competition occurs at a higher carrier density where the radiative rate is faster. The net result is more efficient low-injection performance at the expense of a slightly reduced efficiency when higher-injection levels are applied.

ACKNOWLEDGMENTS

The work at UNCC was supported by ARO/Electronics (Grant No. W911NF-16-1-0263) and at IOS by the National Key Research and Development Program of China (Grant No. 2016YFB0400102) and Guangzhou Science & Technology Project of Guangdong Province, China (Grant Nos. 201704030106 and 2016201604030035).

REFERENCES

- ¹G. Verzellesi, D. Saguatti, M. Meneghini, F. Bertazzi, M. Goano, G. Meneghesso, and E. Zanoni, *J. Appl. Phys.* **114**, 071101 (2013).
- ²J. Cho, E. F. Schubert, and J. K. Kim, *Laser Photonics Rev.* **7**, 408 (2013).
- ³J. Iveland, L. Martinelli, J. Peretti, J. S. Speck, and C. Weisbuch, *Phys. Rev. Lett.* **110**, 177406 (2013).
- ⁴G.-B. Lin, E. Fred Schubert, J. Cho, J. H. Park, and J. K. Kim, *ACS Photonics* **2**, 1013 (2015).
- ⁵H. Y. Ryu, K. H. Ha, J. H. Chae, K. S. Kim, J. K. Son, O. H. Nam, Y. J. Park, and J. I. Shim, *Appl. Phys. Lett.* **89**, 171106 (2006).
- ⁶Q. Dai, M. F. Schubert, M. H. Kim, J. K. Kim, E. F. Schubert, D. D. Koleske, M. H. Crawford, S. R. Lee, A. J. Fischer, G. Thaler, and M. A. Banas, *Appl. Phys. Lett.* **94**, 111109 (2009).
- ⁷S. F. Chichibu, H. Marchand, M. S. Minsky, S. Keller, P. T. Fini, J. P. Ibbetson, S. B. Fleischer, J. S. Speck, J. E. Bowers, E. Hu, U. K. Mishra, S. P. DenBaars, T. Deguchi, T. Sota, and S. Nakamura, *Appl. Phys. Lett.* **74**, 1460 (1999).
- ⁸S. Chichibu, T. Azuhata, T. Sota, and S. Nakamura, *Appl. Phys. Lett.* **69**, 4188 (1996).
- ⁹Y. Lin, Y. Zhang, Z. Liu, L. Su, J. Zhang, and T. Wei, *J. Appl. Phys.* **115**, 0233103 (2014).
- ¹⁰Y. Zhang, M. D. Sturge, K. Kash, B. P. van der Gaag, A. S. Gozdz, L. T. Florez, and J. P. Harbison, *Phys. Rev. B* **51**, 13303 (1995).
- ¹¹W. Shockley and W. T. Read, Jr., *Phys. Rev.* **87**, 835 (1952); R. N. Hall, *ibid.* **87**, 387 (1952).
- ¹²Q. Dai, Q. Shan, J. Wang, S. Chhajed, J. Cho, E. Fred Schubert, M. H. Crawford, D. D. Koleske, M.-H. Kim, and Y. Park, *Appl. Phys. Lett.* **97**, 133507 (2010).
- ¹³F. Nippert, S. Yu, G. C. Karpov, B. Galler, T. Kure, C. Nenstiel, M. R. Wagner, M. Strassburg, H.-J. Lugauer, and A. Hoffmann, *Appl. Phys. Lett.* **109**, 161103 (2016).
- ¹⁴M. A. Hopkins, D. W. E. Allsopp, M. J. Kappers, R. A. Oliver, and C. J. Humphreys, *J. Appl. Phys.* **122**, 234505 (2017).
- ¹⁵T. H. Gfroerer, L. P. Priestley, F. E. Weindruch, and M. W. Wanlass, *Appl. Phys. Lett.* **80**, 4570 (2002).
- ¹⁶T. Saitoh, H. Iwadate, and H. Hasegawa, *Jpn. J. Appl. Phys.* **30**(1), 3750 (1991).
- ¹⁷J. Xie, X. Ni, Q. Fan, R. Shimada, U. Ozgur, and H. Morkoc, *Appl. Phys. Lett.* **93**, 121107 (2008).
- ¹⁸D.-P. Han, D.-G. Zheng, C.-H. Oh, H. Kim, J.-I. Shim, D.-S. Shin, and K.-S. Kim, *Appl. Phys. Lett.* **104**, 151108 (2014).
- ¹⁹T. H. Gfroerer, B. Stroup, Y. Zhang and Z. Liu, in *Proceedings of the 7th World Conference on Photovoltaic Energy Conversion* (IEEE, 2018), p. 3248.
- ²⁰D.-P. Han, J.-I. Shim, and D.-S. Shin, *Appl. Phys. Express* **10**, 052101 (2017).
- ²¹P. Kivisaari, L. Riuttanen, J. Oksanen, S. Suihkonen, M. Ali, H. Lipsanen, and J. Tulkki, *Appl. Phys. Lett.* **101**, 021113 (2012).
- ²²T. H. Gfroerer, Y. Zhang, and M. W. Wanlass, *Appl. Phys. Lett.* **102**, 012114 (2013).
- ²³T. J. Badcock, M. Ali, T. Zhu, M. Pristovsek, R. A. Oliver, and A. J. Shields, *Appl. Phys. Lett.* **109**, 151110 (2016).
- ²⁴R. K. Arhenkiel, B. M. Keyes, G. B. Lush, M. R. Melloch, M. S. Lundstrom, and H. F. MacMillan, *J. Vac. Sci. Technol. A* **10**, 990 (1992).
- ²⁵R. K. Arhenkiel, *Semicond. Semimetals* **39**, 39–150 (1993).
- ²⁶T. H. Gfroerer, L. P. Priestley, M. F. Fairley, and M. W. Wanlass, *J. Appl. Phys.* **94**, 1738 (2003).
- ²⁷T. Matsusue and H. Sakaki, *Appl. Phys. Lett.* **50**, 1429 (1987).
- ²⁸M. W. Gerber and R. N. Kleinman, *J. Appl. Phys.* **121**, 225702 (2017).
- ²⁹J. Hader, J. V. Moloney, and S. W. Koch, *Appl. Phys. Lett.* **99**, 181127 (2011).
- ³⁰F. Urbach, *Phys. Rev.* **69**, 1324 (1953).